Supporting Information for

Synergetic magnetic and luminescence switching via thermo-induced solid state phase transitions of dysprosium-dianthracene complex

Jing-Cui Liu,[a,†] Xin-Da Huang,[a,†] Qian Zou,[a] Song-Song Bao,[a] Xi-Zhang Wang,[b] Jing-Yuan Ma,[c] Li-Min Zheng*,[a]

[a] State Key Laboratory of Coordination Chemistry, School of Chemistry and Chemical Engineering, Collaborative Innovation Center of Advanced Microstructures, Nanjing University, Nanjing 210023, P. R. China

[b] Key Laboratory of Mesoscopic Chemistry of MOE, School of Chemistry and Chemical Engineering, Nanjing University, Nanjing 210023, P. R. China

[c] Shanghai Synchrotron Radiation Facility, Chinese Academia Science, Shanghai 201204, P. R. China

*correspondence to: lmzheng@nju.edu.cn

Table S1. Selected bond lengths (Å) and angles (°) for 1-Ln and 1-Dy-170-2min.

Sample	1-Dy	1-Dy-170-2min	1-Gd
Ln1-Cl1	2.6454(11)	2.6485(19)	2.6741(14)
Ln1-O1	2.277(2)	2.288(5)	2.300(4)
Ln1-O4	2.196(3)	2.199(5)	2.229(4)
Ln1-O5	2.201(2)	2.198(5)	2.223(4)
Ln1-N1	2.555(3)	2.557(6)	2.590(4)
Ln1-N2	2.527(3)	2.526(5)	2.550(5)
Ln1-N3	2.540(3)	2.540(7)	2.576(4)
C6-C13	1.636(5)	2.433(2)	1.652(7)
Cl1-Ln1-O1	164.60(6)	165.67(14)	164.00(10)
Cl1-Ln1-O4	98.02(7)	98.23(15)	98.24(10)
Cl1-Ln1-O5	97.66(7)	97.71(14)	98.07(11)
Cl1-Ln1-N1	90.30(7)	91.48(14)	90.55(11)
Cl1-Ln1-N2	84.24(7)	85.53(13)	83.90(12)
Cl1-Ln1-N3	87.78(7)	87.94(17)	87.68(10)
O1-Ln1-O4	95.56(9)	94.4(2)	95.93(14)
O1-Ln1-O5	91.22(9)	90.7(2)	90.71(14)
O1-Ln1-N1	87.12(9)	86.1(2)	87.11(15)
O1-Ln1-N2	80.82(9)	80.54(18)	80.67(15)
O1-Ln1-N3	82.99(9)	83.6(2)	82.39(14)
O4-Ln1-O5	82.69(9)	82.3(2)	84.21(14)
O4-Ln1-N1	71.61(9)	71.5(2)	70.74(15)
O4-Ln1-N2	137.89(9)	138.0(2)	137.02(14)
O4-Ln1-N3	154.72(9)	154.3(2)	155.81(14)
O5-Ln1-N1	153.94(9)	153.28(19)	154.46(15)
O5-Ln1-N2	138.98(9)	138.91(19)	138.31(14)
O5-Ln1-N3	72.13(9)	72.2(2)	71.72(14)
N1-Ln1-N2	66.32(9)	66.58(19)	66.30(15)
N1-Ln1-N3	133.23(9)	133.5(2)	132.93(14)
N2-Ln1-N3	66.99(9)	67.0(2)	66.75(13)

Table S2. Coordination geometry for compounds **1-Ln** and **1-Dy-170-2min** at 173K.

Coordination geometry	1-Dy	1-Dy-170-2min	1-Gd
Heptagon (D_{7h})	34.43	34.558	34.21
Hexagonal pyramid (C_{6v})	24.93	25.167	24.87
Pentagonal bipyramid (D_{5h})	**0.538**	**0.554**	**0.600**
Capped octahedron (C_{3v})	8.025	8.017	7.964
Capped trigonal prism (C_{2v})	6.553	6.577	6.533
Johnson pentagonal bipyramid J13 (D_{5h})	4.448	4.523	4.475
Johnson elongated triangular pyramid J7 (C_{3v})	24.04	24.102	23.93

Table S3. Forward Fourier Transform and backward Fourier Transform selected parameters of the Dy-N/O/Cl shell at Dy-L$_3$ edge of **1-Dy** and the related complexes.

Sample	Shell	*K*-range	Window type	*R*-range	Window type
1-Dy	Dy-O/N/Cl	2.772 – 11.425	Hanning	1.25 – 2.51	Hanning
2-Dy	Dy-O/N/Cl	2.772 – 11.425	Hanning	1.25 – 2.53	Hanning
3-Dy	Dy-O/N	2.788 – 11.425	Hanning	1.20 – 2.53	Hanning

Table S4. Forward Fourier Transform and backward Fourier Transform selected parameters of the Gd-N/O/Cl shell at Gd-L$_3$ edge of **1-Gd** and the related complexes.

Sample	Shell	*K*-range	Window type	*R*-range	Window type
1-Gd	Gd-O/N/Cl	2.793 – 11.300	Hanning	1.25 – 2.56	Hanning
2-Gd	Gd-O/N/Cl	2.835 – 11.300	Hanning	1.25 – 2.55	Hanning
3-Gd	Gd-O/N	2.811 – 11.300	Hanning	1.25 – 2.54	Hanning

Table S5. Local structural fitting parameters of the Gd-O, Gd-N and Gd-Cl shells around Gd.

Sample	Shell	*R*	*N*	$S_0^{2\,b}$	ΔE_0	ΔR	σ^2	*R*-factor [a]
1-Gd	Gd-O	2.24	**3**	1.0	4.1 ± 1.8	0.010 ± 0.008	0.0072 ± 0.0028	
	Gd-N	2.44	**3**	1.0	5.8 ± 1.1	-0.12 ± 0.01	0.0067 ± 0.0061	0.0012
	Gd-Cl	2.69	**1**	1.0	-2.4 ± 2.9	0.0088 ± 0.0086	0.0014 ± 0.0010	
2-Gd	Gd-O	2.24	**3**	1.0	3.4 ± 2.2	0.0096 ± 0.0068	0.0080 ± 0.0024	
	Gd-N	2.45	**3**	1.0	7.0 ± 1.4	-0.11 ± 0.01	0.011 ± 0.008	0.0059
	Gd-Cl	2.67	**0.9**	1.0	-3.6 ± 2.4	0.00± 0.01	0.0014 ± 0.0005	
3-Gd	Gd-O	2.28	**4**	1.0	7.6 ± 0.5	0.055 ± 0.004	0.0059 ± 0.0007	0.0070
	Gd-N	2.54	**3**	1.0	8.4 ± 0.8	-0.019± 0.007	0.0033 ± 0.0010	

[a] *R*-factor by *k*-weight = 2; [b] fixed to 1.0.

Table S6. The fit parameters obtained from analyses of the ac susceptibilities of **1-Dy** under 500 Oe bias field.

T / K	χ_T / cm^3 mol^{-1}	χ_S / cm^3 mol^{-1}	τ / 10^{-4} s	α	Residual
1.8	4.15	1.52	9.77	0.084	0.051
2.0	3.75	1.42	7.46	0.073	0.025
2.2	3.43	1.32	5.41	0.064	0.017
2.4	3.18	1.22	3.67	0.065	0.012
2.6	2.97	1.09	2.37	0.078	0.015
2.8	2.77	0.88	1.36	0.010	0.010
3.0	2.60	0.47	0.68	0.112	0.004
3.2	2.45	0	0.36	0.100	0.006

Table S7. The relaxation parameters for all dysprosium samples.

Compounds	U_{eff} / K	τ_0 / s	C / s^{-1} K^{-n}	n
1-Dy	39.0	2.2 x 10^{-10}	196	2.8
2-Dy	14.6	1.5 x 10^{-7}		
3-Dy	14.7	1.4 x 10^{-7}		
1-Dy-170-2min	14.8	9.6 x 10^{-8}		
1-Dy'	40.1	9.1 x 10^{-11}	311	2.4

Table S8. The fit parameters obtained from analyses of the ac susceptibilities of **1-Dy'** under 500 Oe bias field.

T / K	χ_T / cm^3 mol^{-1}	χ_S / cm^3 mol^{-1}	τ / 10^{-4} s	α	Residual
1.8	4.06	1.62	7.89	0.08	0.17
2.0	3.70	1.52	6.25	0.07	0.06
2.2	3.41	1.42	4.60	0.07	0.04
2.4	3.14	1.31	3.13	0.06	0.02
2.6	2.94	1.08	1.86	0.11	0.05
2.8	2.72	0.89	1.11	0.10	0.05
3.0	2.57	0.09	0.43	0.15	0.02
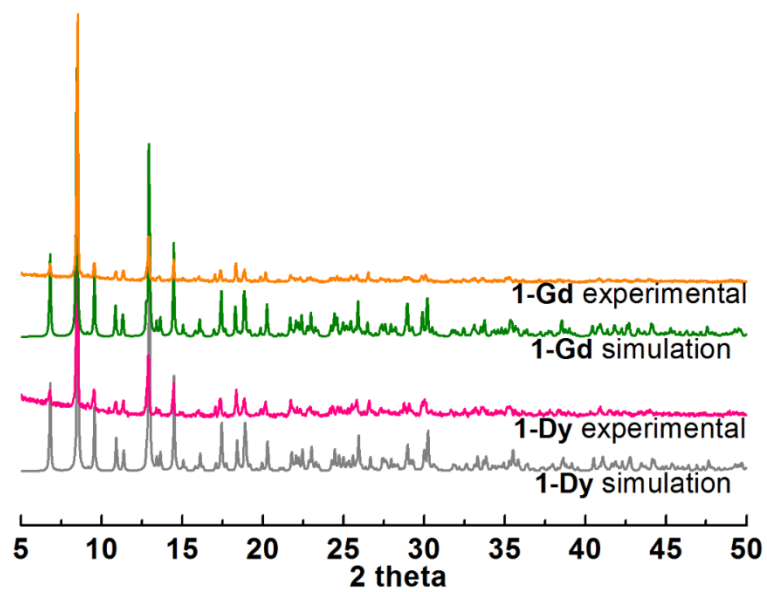
Figure S1. Experimental and simulated XRD patterns of compounds **1-Ln** (Ln = Gd, Dy).
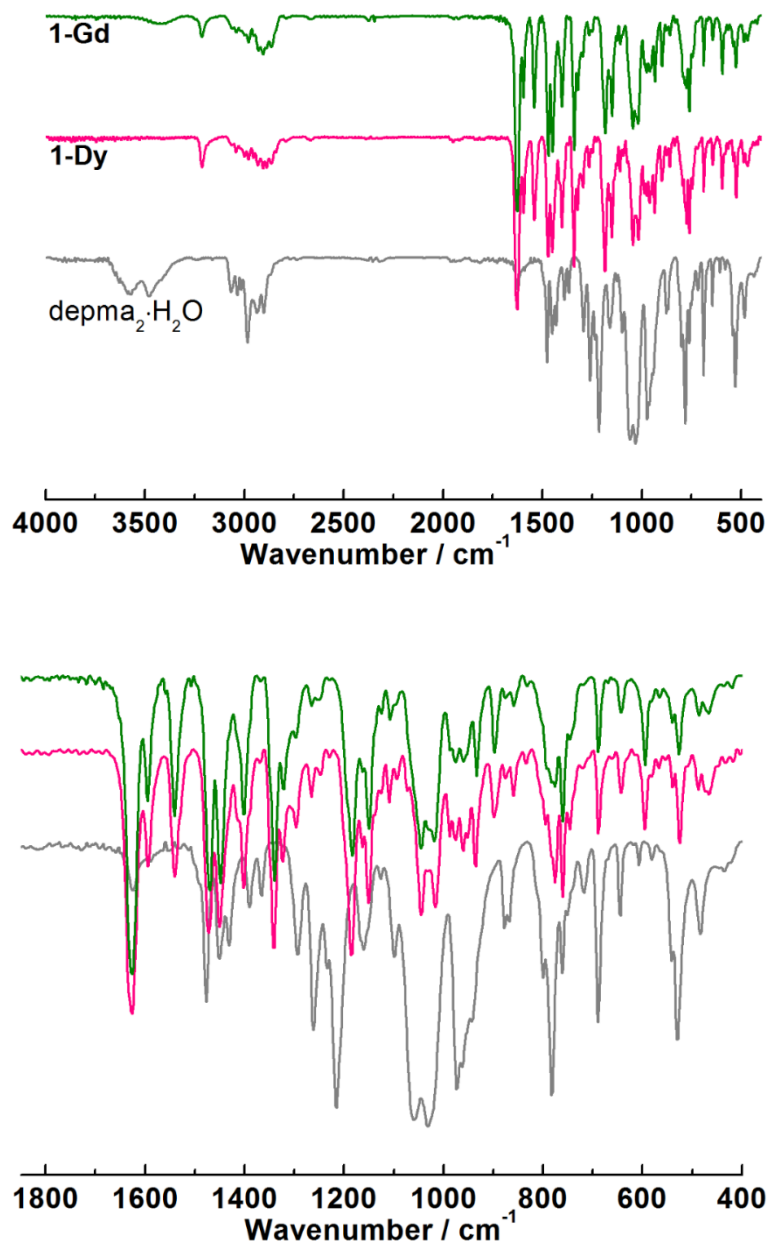
Figure S2. Infrared spectra of depma$_2$·H$_2$O and compounds **1-Ln** (Ln = Gd, Dy).
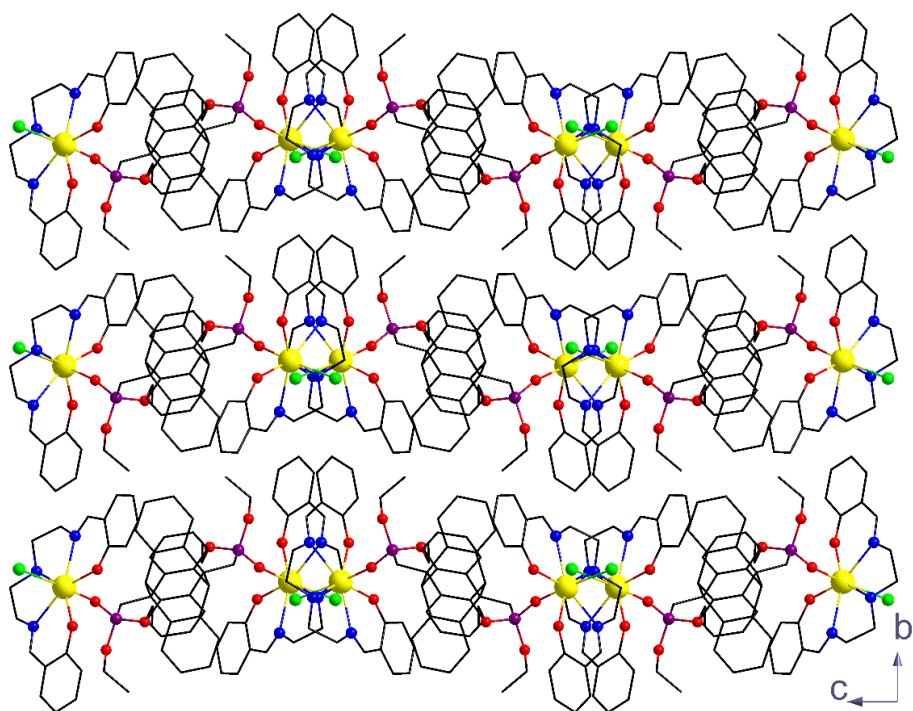
Figure S3. Packing diagram of compound **1-Dy** viewed along the a-axis.
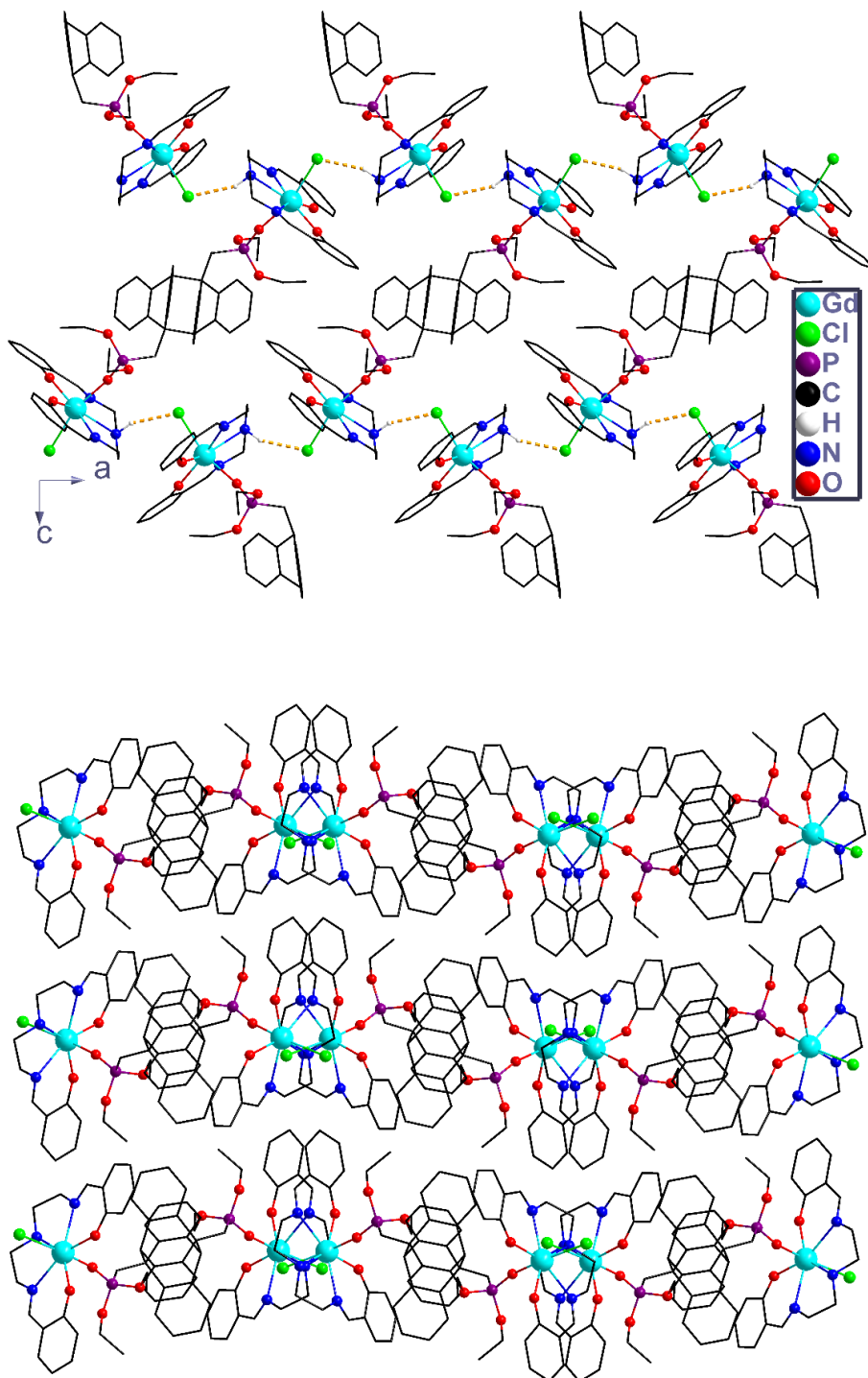
Figure S4. Layer structure of compound **1-Gd** formed by hydrogen bond (top); Packing diagram of compound **1-Gd** viewed along the a-axis (bottom).
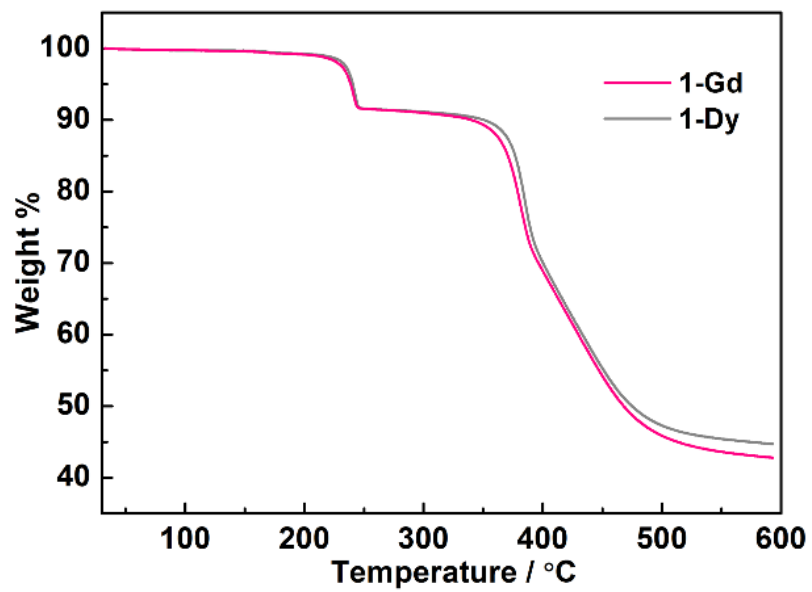
Figure S5. Thermogravimetric analysis for compounds **1-Ln**.
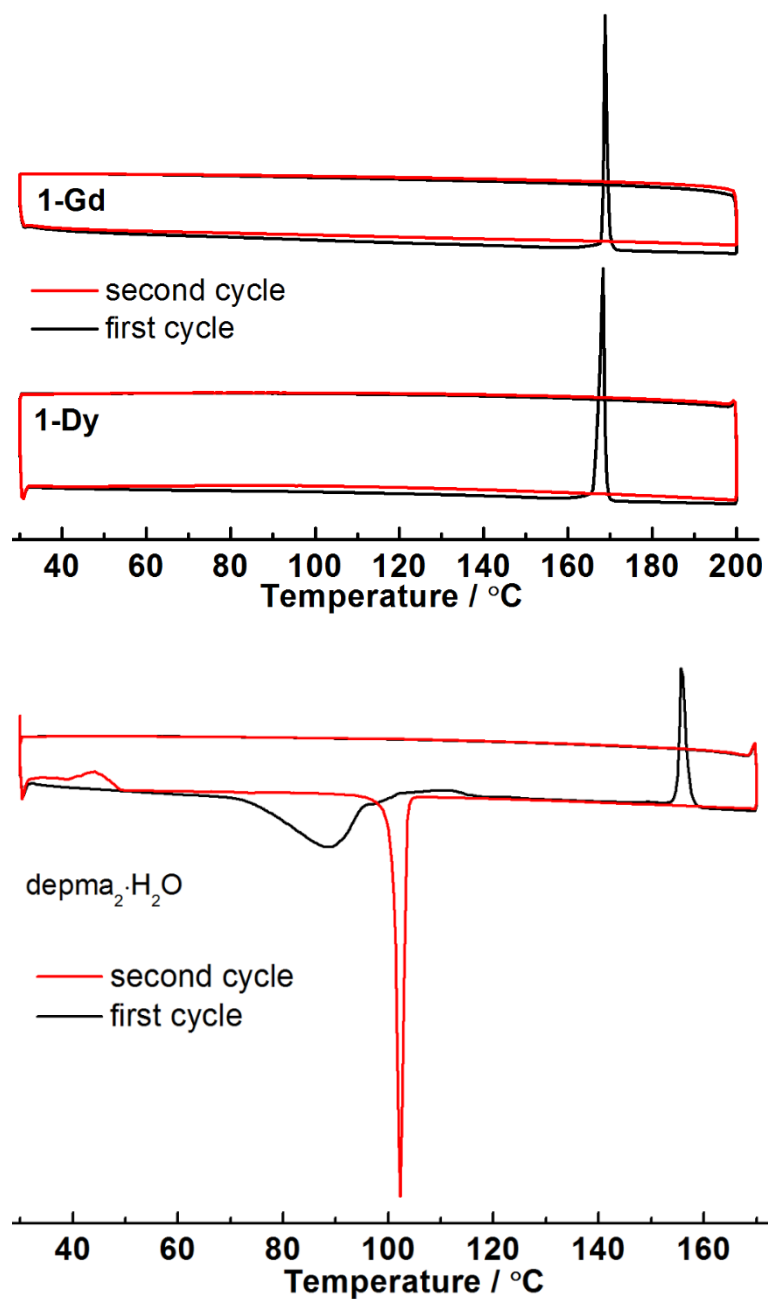
Figure S6. DSC curves for compounds **1-Ln** in the temperature range 30 – 200 °C (top) and depma$_2$·H$_2$O (bottom) tested at a heating rate of 5 °C/min (black curve for the first cycle, red curve for the second cycle).
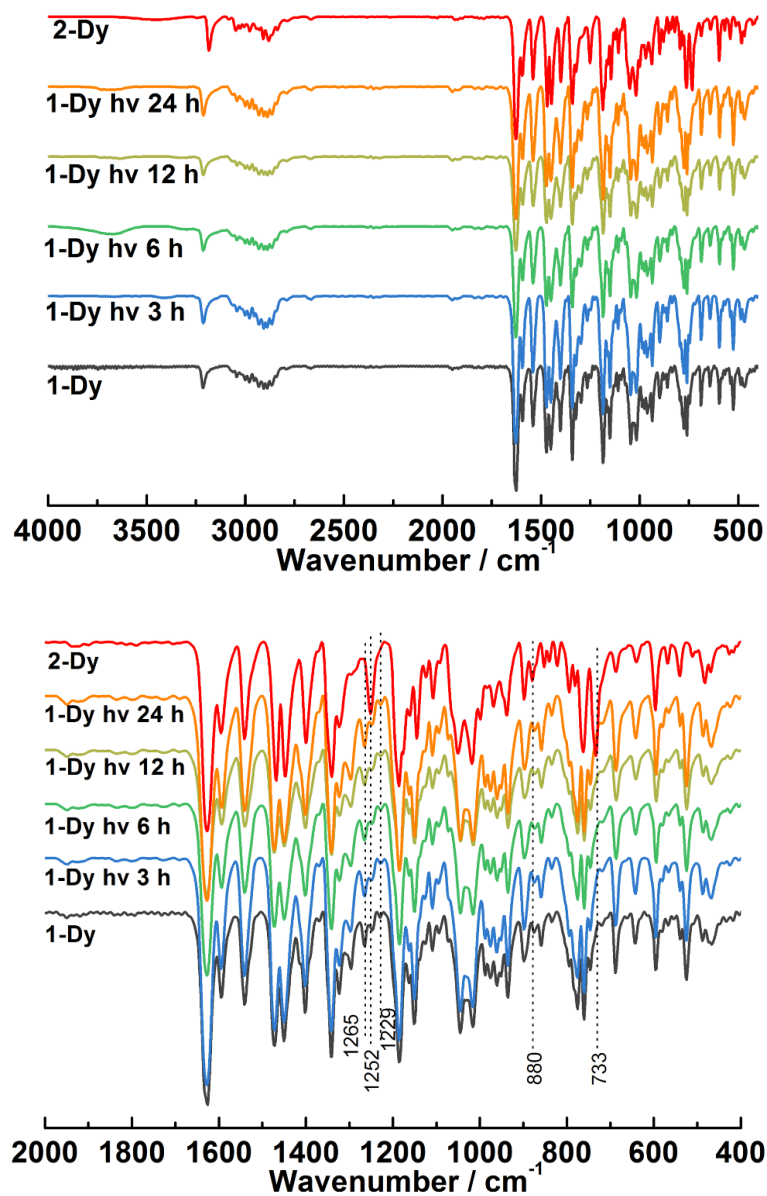
Figure S7. IR spectra for compound **1-Dy** before and after light irradiation at 254 nm for different period of time. The IR spectrum of **2-Dy** is also presented for comparison.
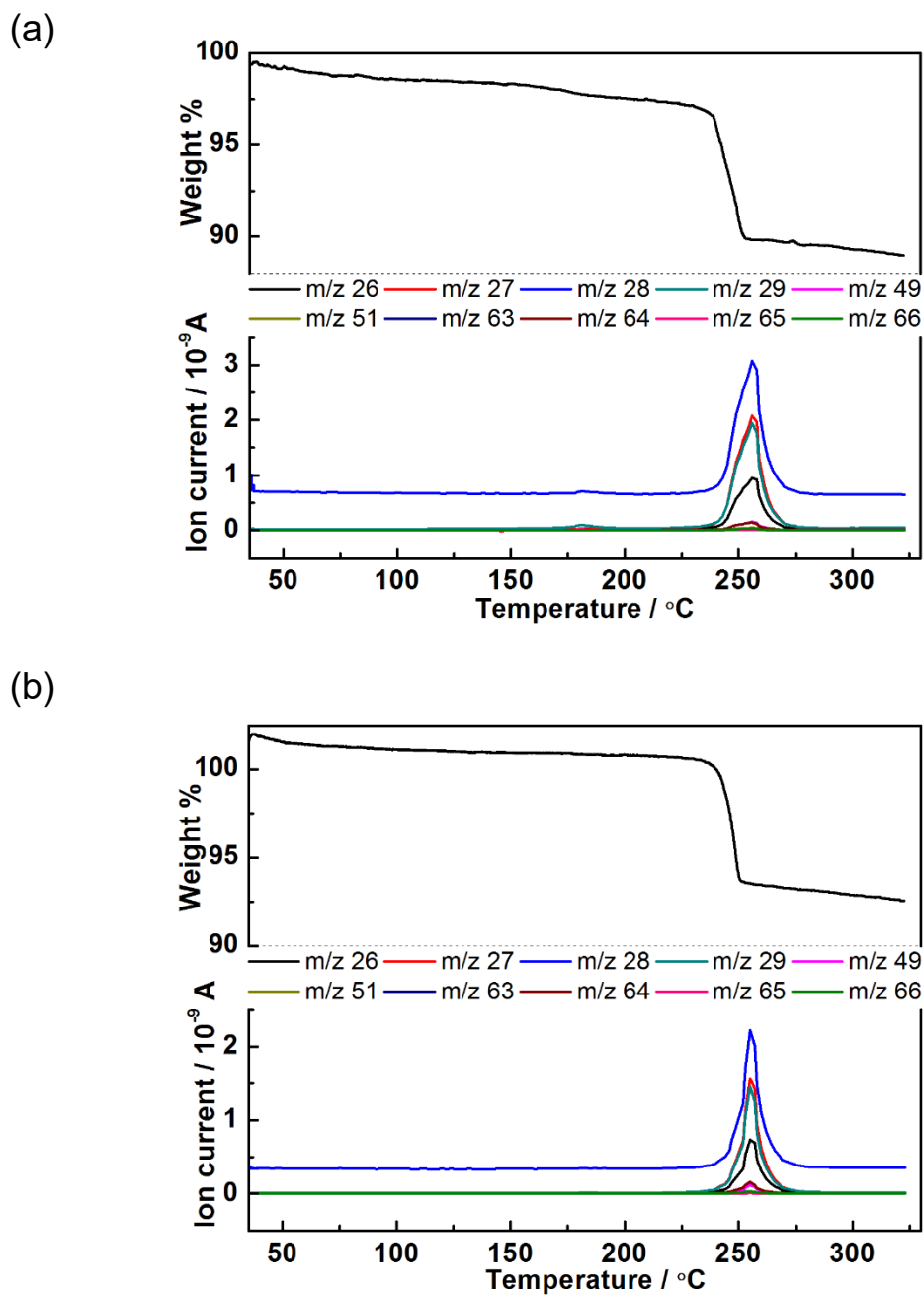
Figure S8. TG-MS curves for compounds **1-Dy** (a) and **1-Gd** (b). The assignment of the peaks: m/z 26, C_2H_2; m/z 27, C_2H_3; m/z 28, C_2H_4; m/z 29, C_2H_5; m/z 49, $CH_2{}^{35}Cl$; m/z 51, $CH_2{}^{37}Cl$; m/z 63, $CH_2CH_2{}^{35}Cl$; m/z 64, $CH_3CH_2{}^{35}Cl$; m/z 65, $CH_2CH_2{}^{37}Cl$; m/z 66, $CH_3CH_2{}^{37}Cl$.

1-Dy

Element	Wt%	At%
CK	65.11	82.74
NK	04.35	04.74
OK	08.60	08.21
PK	02.81	01.39
ClK	03.35	01.44
DyL	15.77	01.48
Matrix	Correction	ZAF

2-Dy

Element	Wt%	At%
CK	62.81	82.26
NK	03.78	04.24
OK	08.73	08.58
PK	03.26	01.66
ClK	03.44	01.52
DyL	18.00	01.74
Matrix	Correction	ZAF

3-Dy

Element	Wt%	At%
CK	61.70	84.46
NK	02.80	03.28
OK	07.30	07.50
PK	04.19	02.22
ClK	00.30	00.14
DyL	23.72	02.40
Matrix	Correction	ZAF
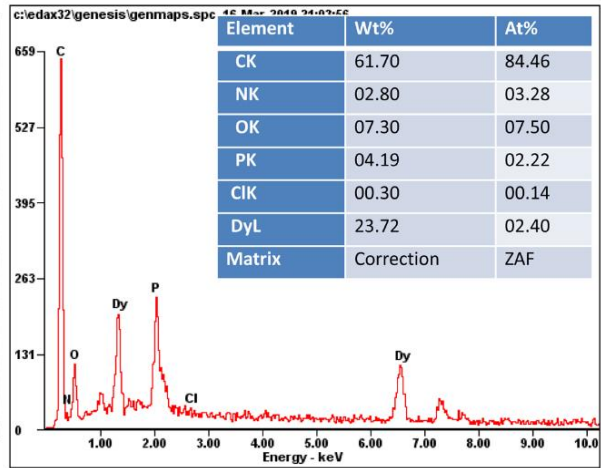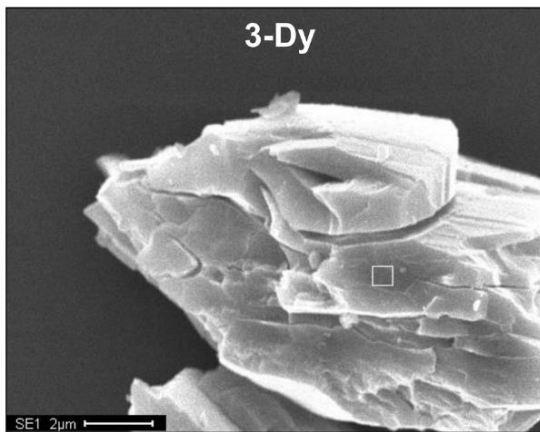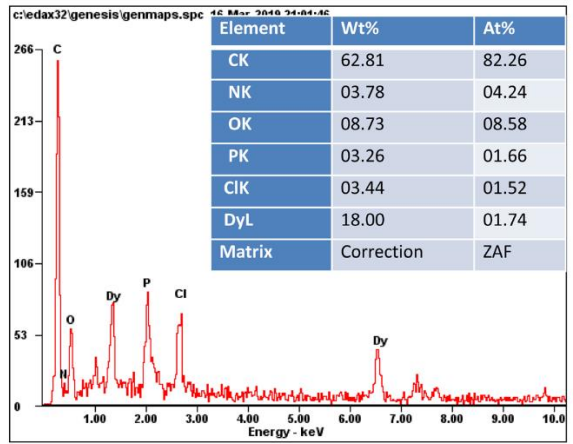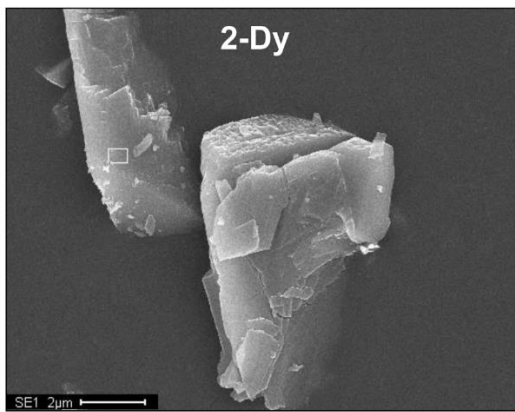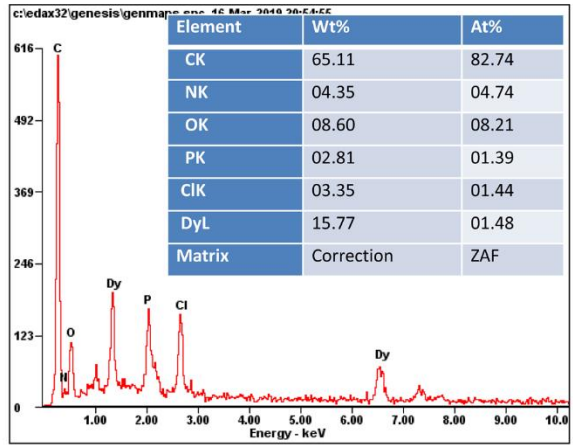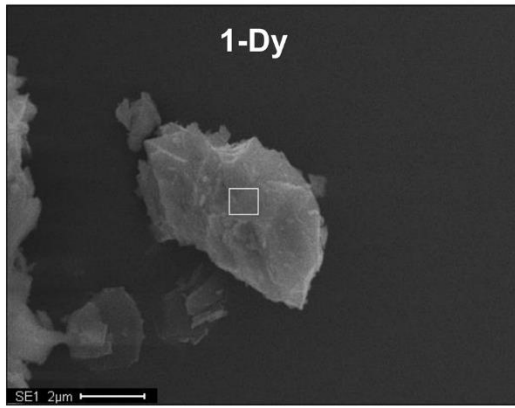
Figure S9. EDX spectra of **1-Dy**, **2-Dy** and **3-Dy**.

Element	Wt%	At%
CK	51.13	80.78
NK	02.95	04.00
OK	04.21	04.99
PK	05.49	03.36
ClK	06.02	03.22
GdL	30.19	03.64
Matrix	Correction	ZAF

Element	Wt%	At%
CK	59.92	85.98
OK	05.85	06.30
PK	04.78	02.66
ClK	04.86	02.36
GdL	24.59	02.70
Matrix	Correction	ZAF

Element	Wt%	At%
CK	66.37	86.36
OK	09.62	09.40
PK	04.28	02.16
ClK	00.36	00.16
GdL	19.37	01.92
Matrix	Correction	ZAF
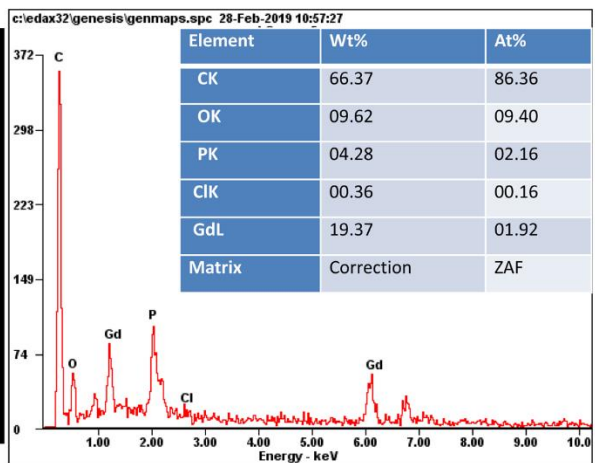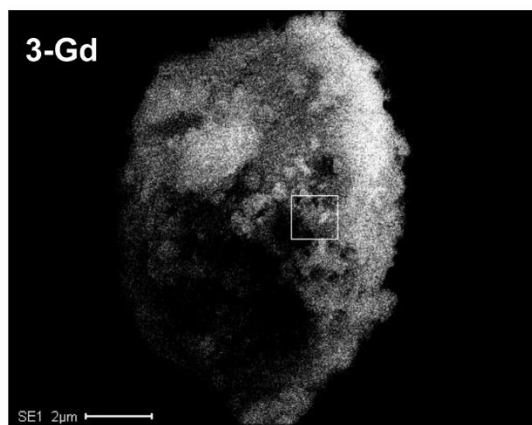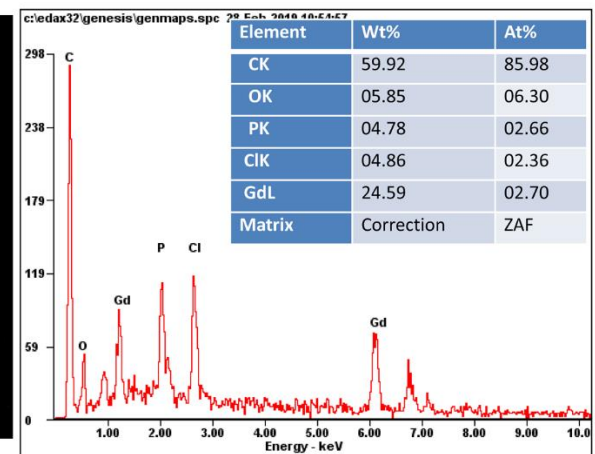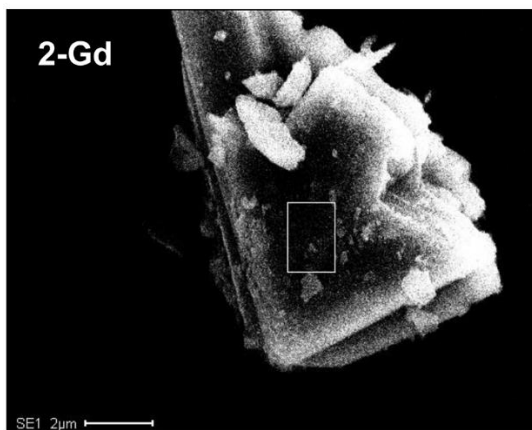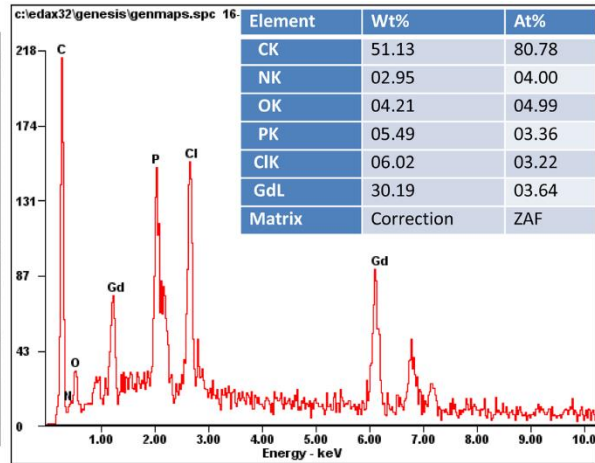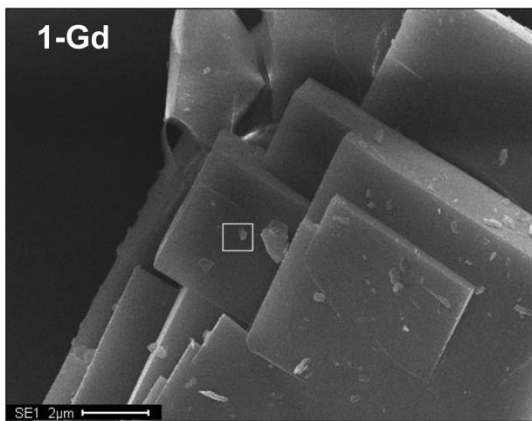
Figure S10. EDX spectra of **1-Gd**, **2-Gd** and **3-Gd**.
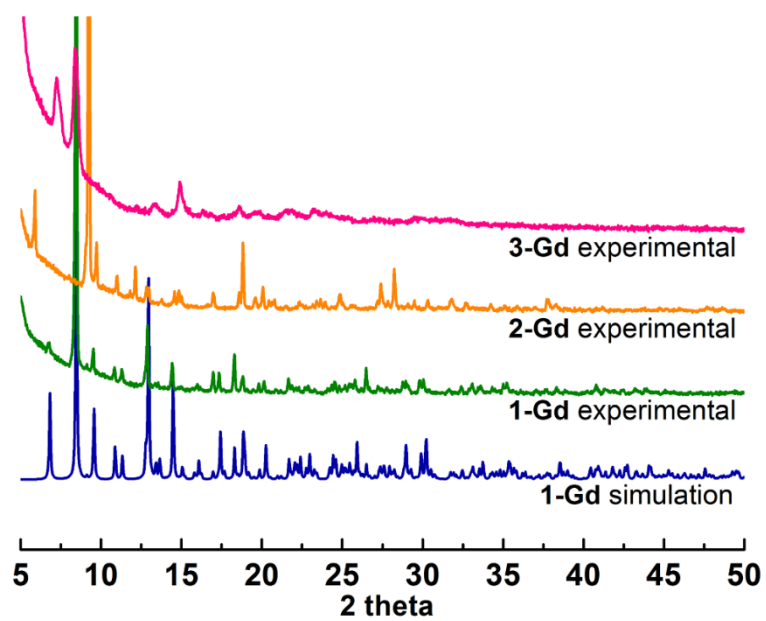
Figure S11. PXRD patterns of **1-Gd**, **2-Gd** and **3-Gd**.
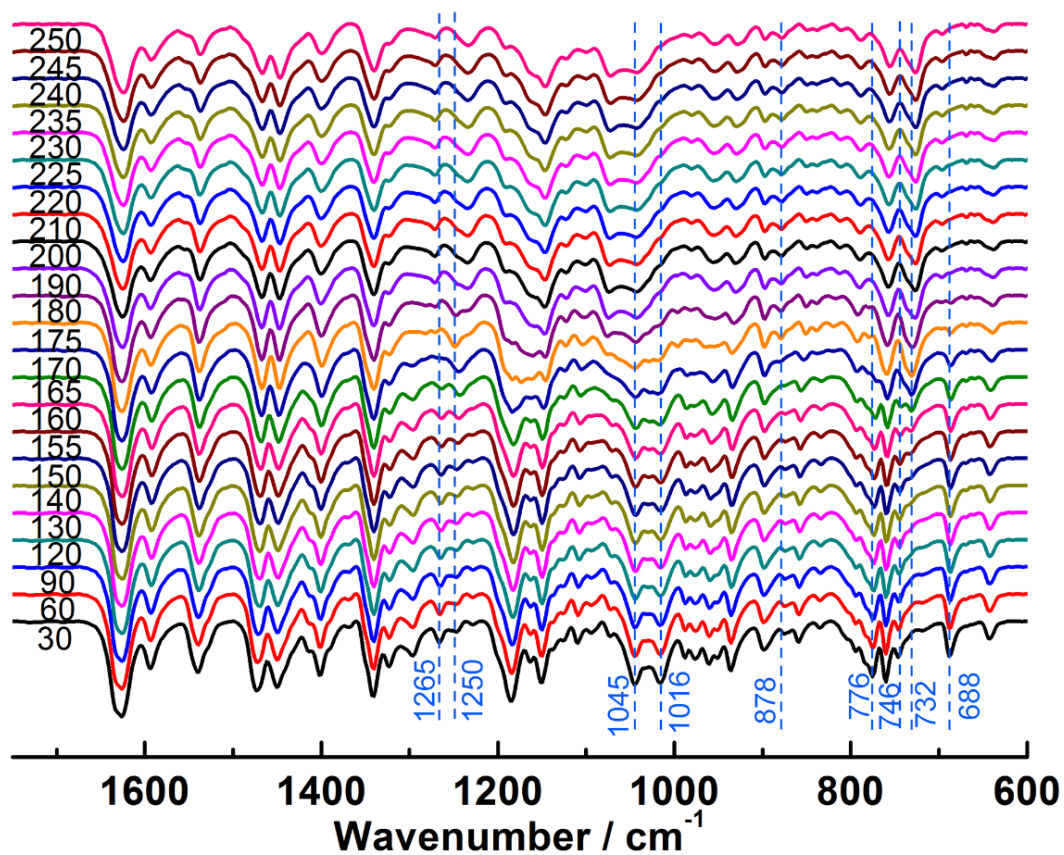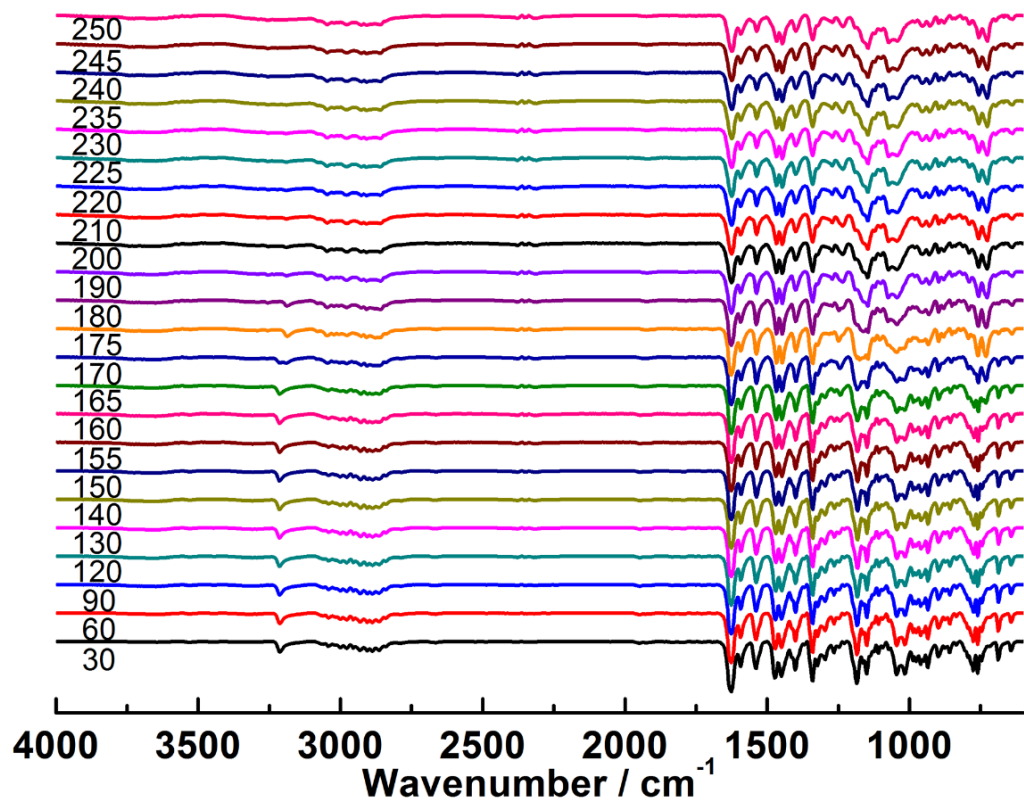
Figure S12. Variable temperature IR spectra for compound **1-Dy**.
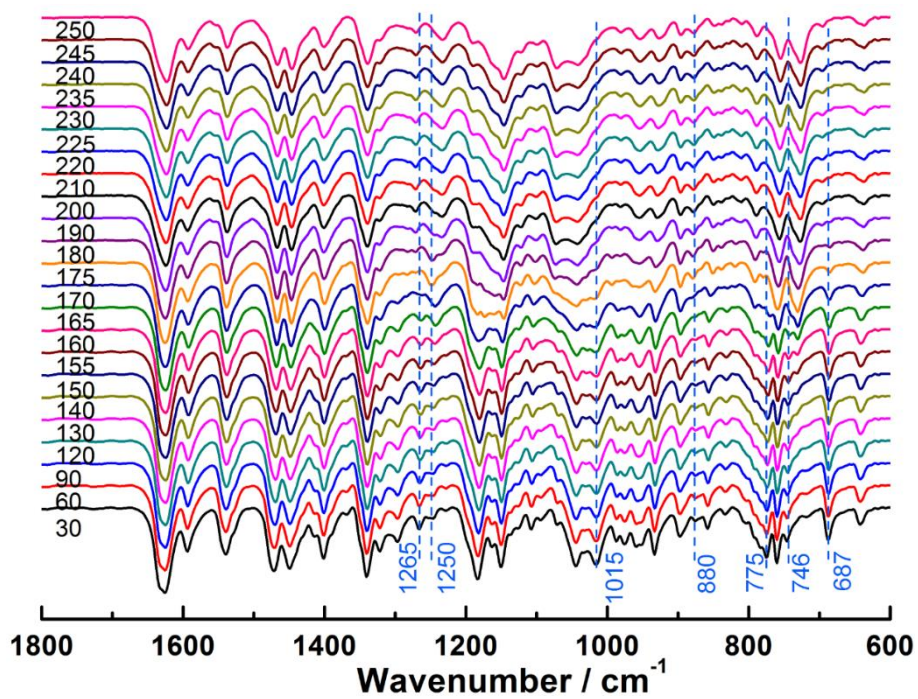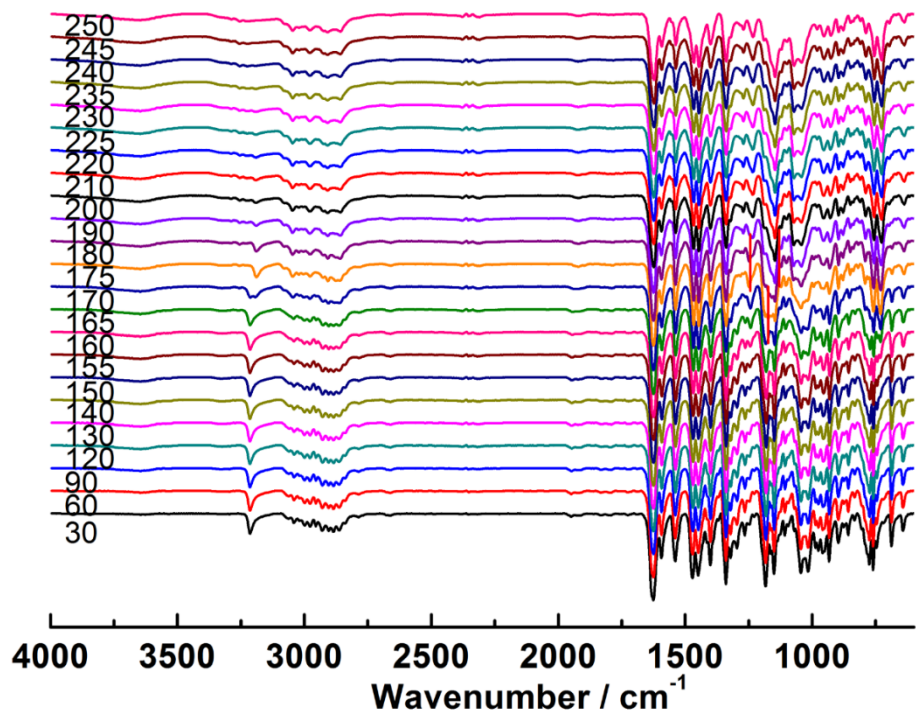
Figure S13. Variable temperature IR spectra for compound **1-Gd**.
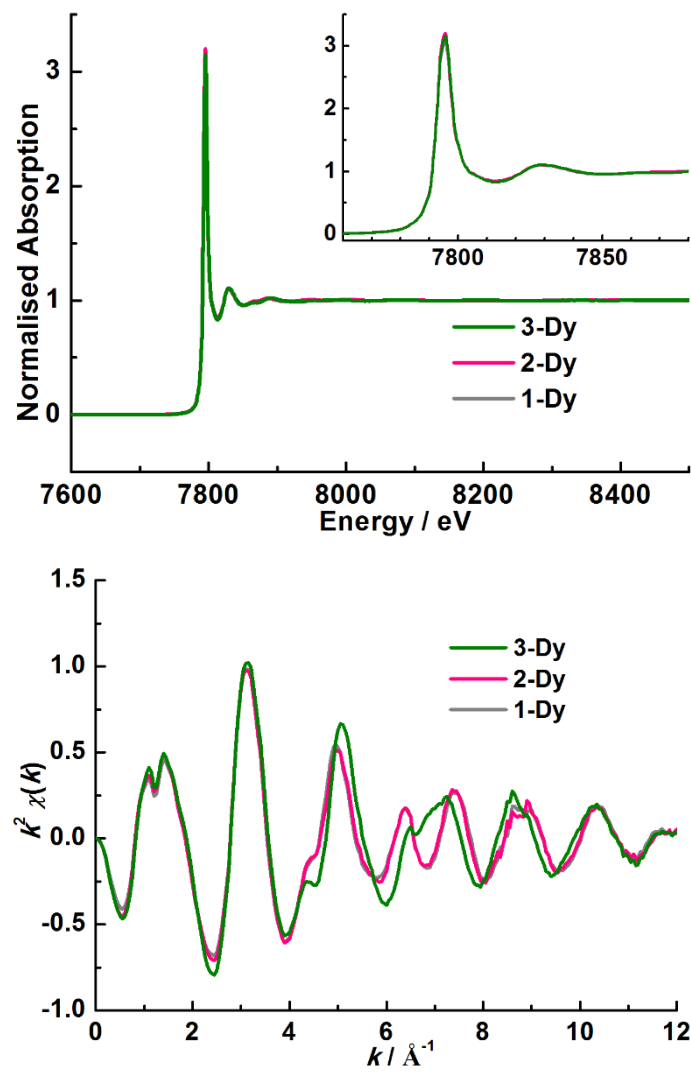
Figure S14. The XANES spectra (top) and k^2-weight EXAFS signals (bottom) at Dy L$_3$-edge for samples **1-Dy**, **2-Dy** and **3-Dy**.
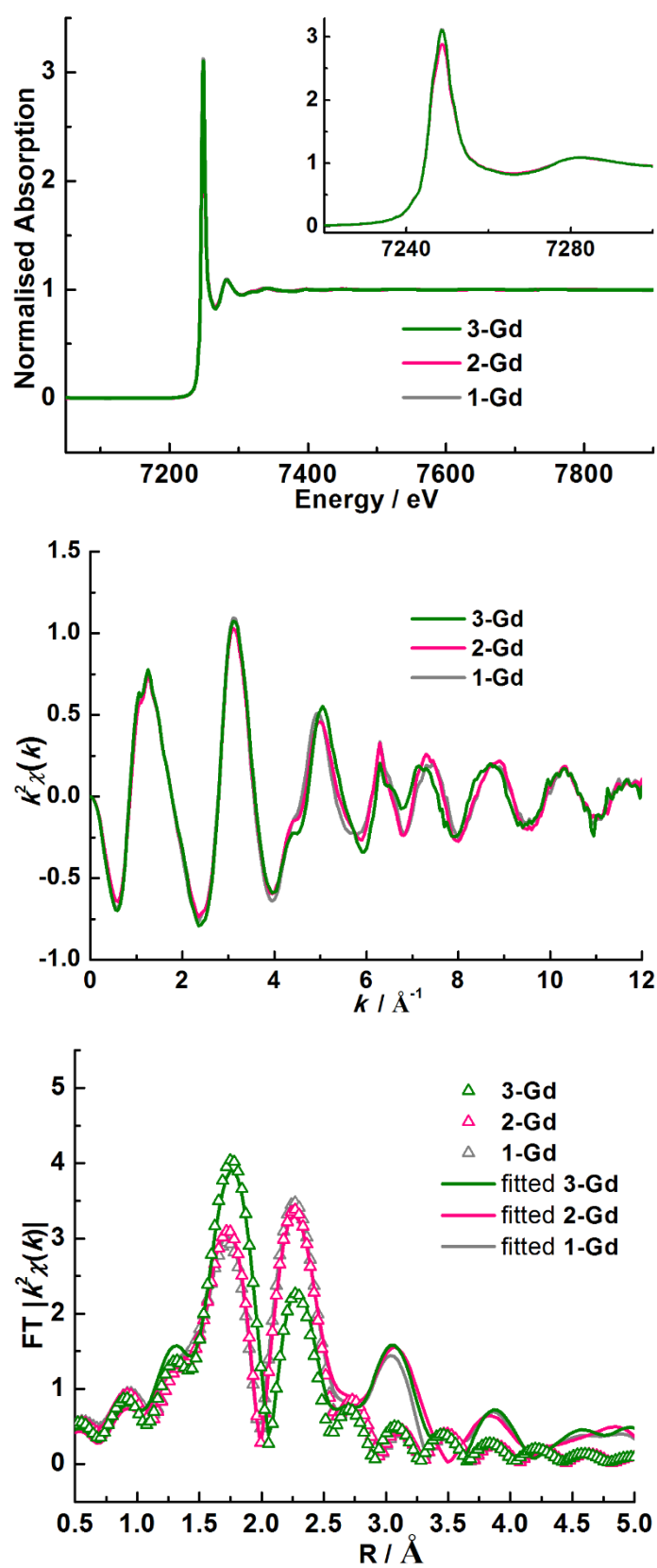
Figure S15. The XANES spectra (top), k^2-weight EXAFS signals (middle) and Fourier transformed space (R space) (bottom) at Gd L$_3$-edge for samples **1-Gd**, **2-Gd** and **3-Gd**.
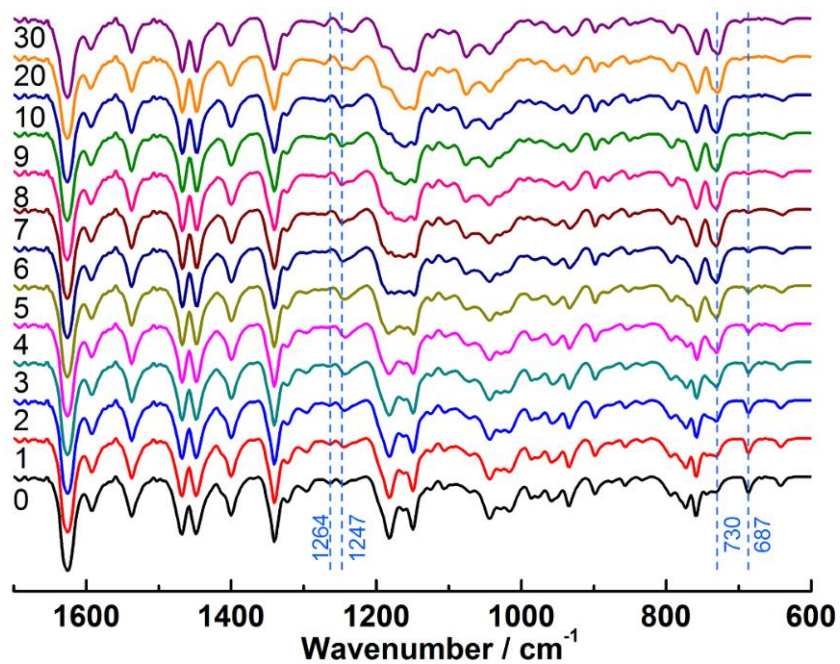
Figure S16. In-situ infrared spectra of compound **1-Dy** at 170 °C (heating time varied from 0 to 30 minutes).
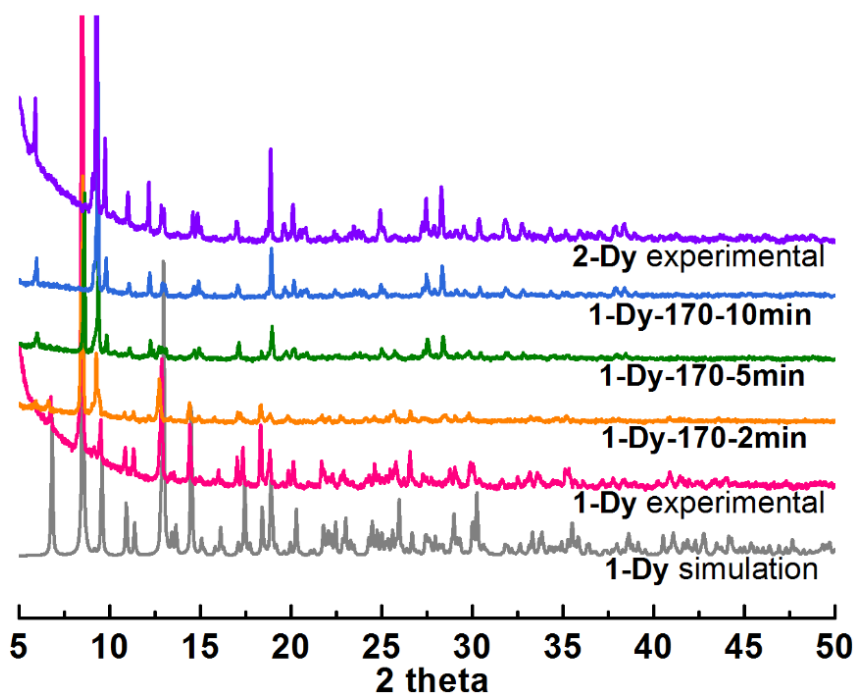
Figure S17. PXRD patterns of **1-Dy**, **1-Dy-170-2min**, **1-Dy-170-5min**, **1-Dy-170-10min** and **2-Dy**.
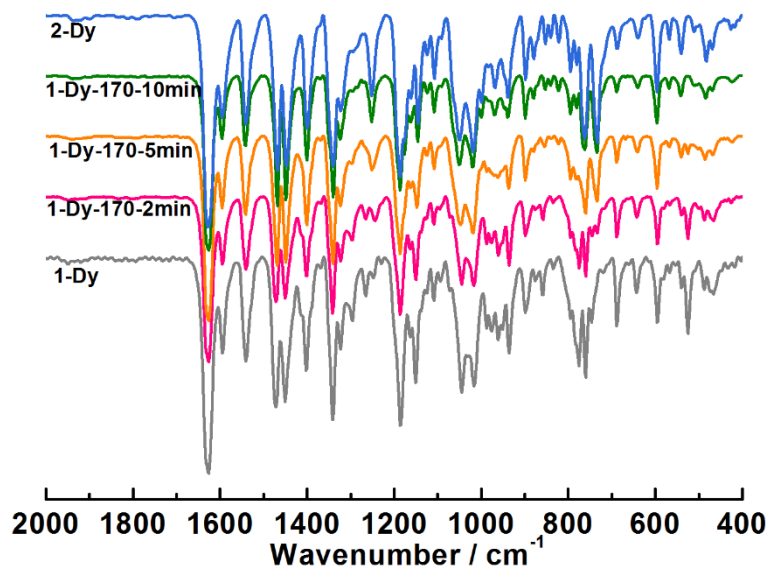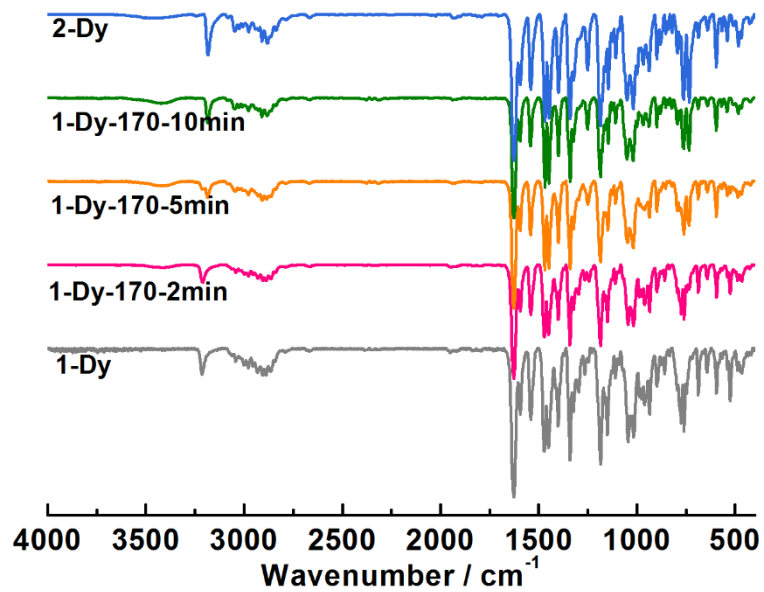
Figure S18. Infrared spectra of compounds **1-Dy**, **1-Dy-170-2min**, **1-Dy-170-5min**, **1-Dy-170-10min** and **2-Dy**.
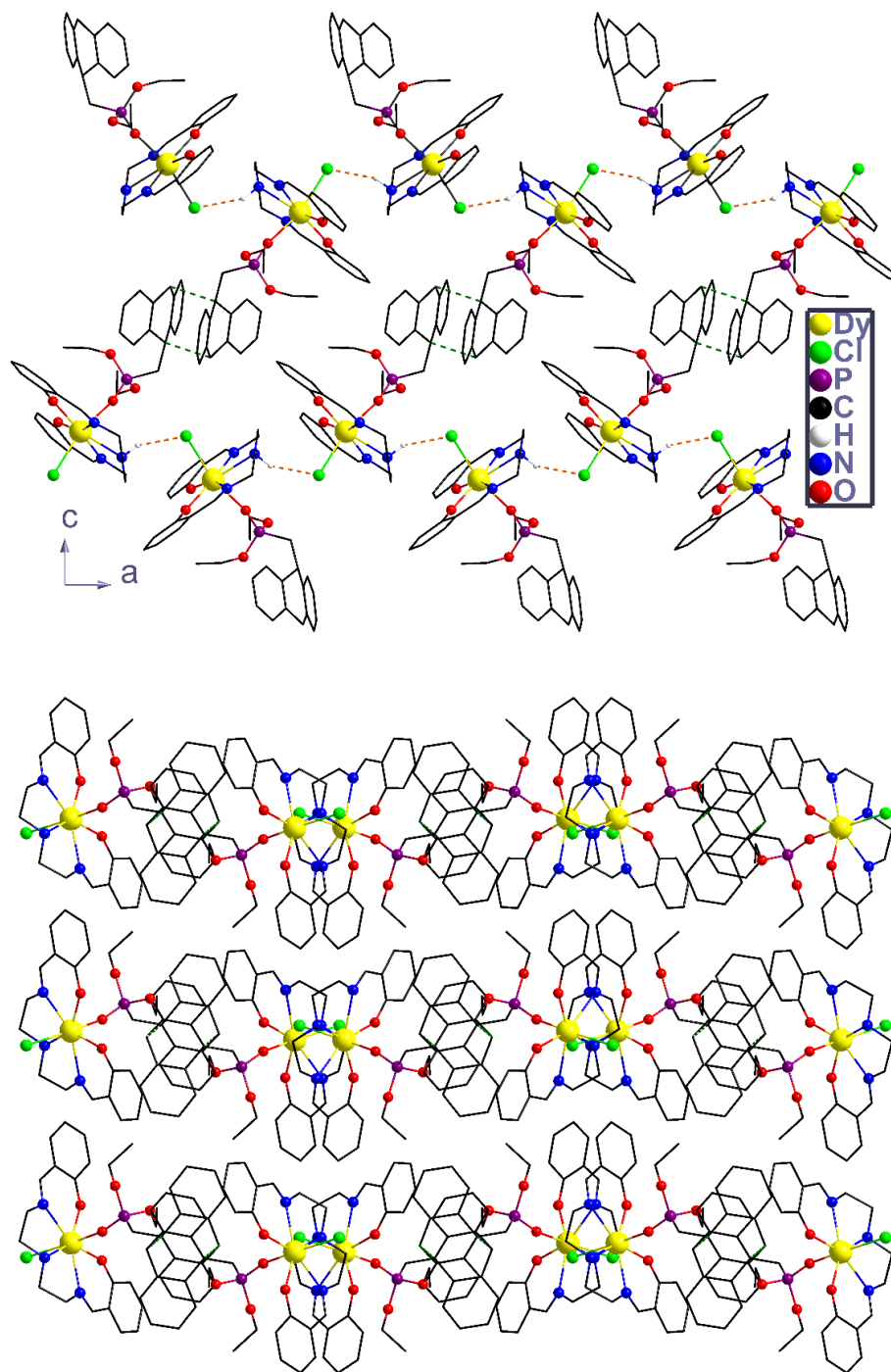
Figure S19. Layer structure of compound **1-Dy-170-2min** formed by hydrogen bond (top); Packing diagram of compound **1-Dy-170-2min** viewed along the a-axis (bottom).
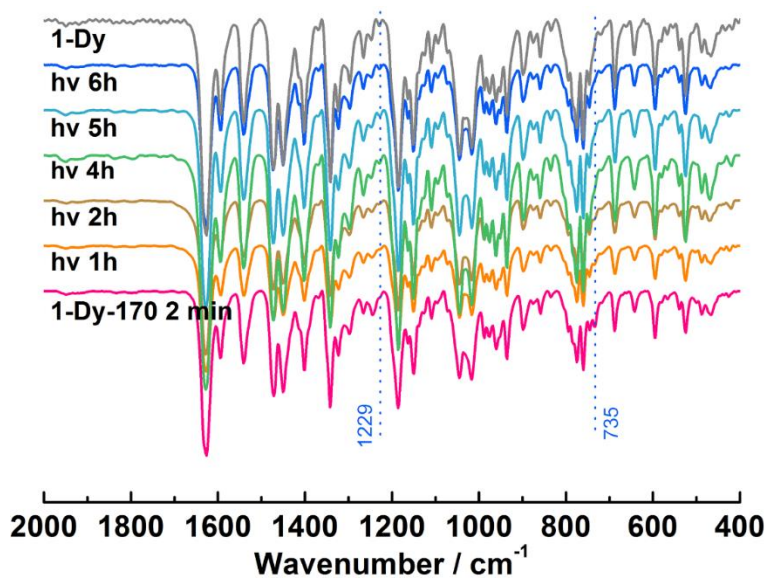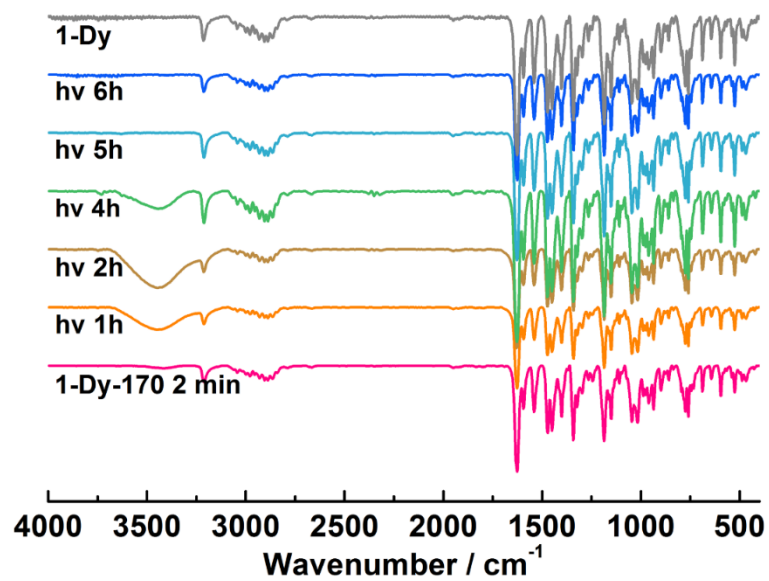
Figure S20. IR spectra of **1-Dy** (grey), **1-Dy-170-2min** (pink) and **1-Dy-170-2min** after UV light (λ = 365 nm) irradiation for 1-6 h.
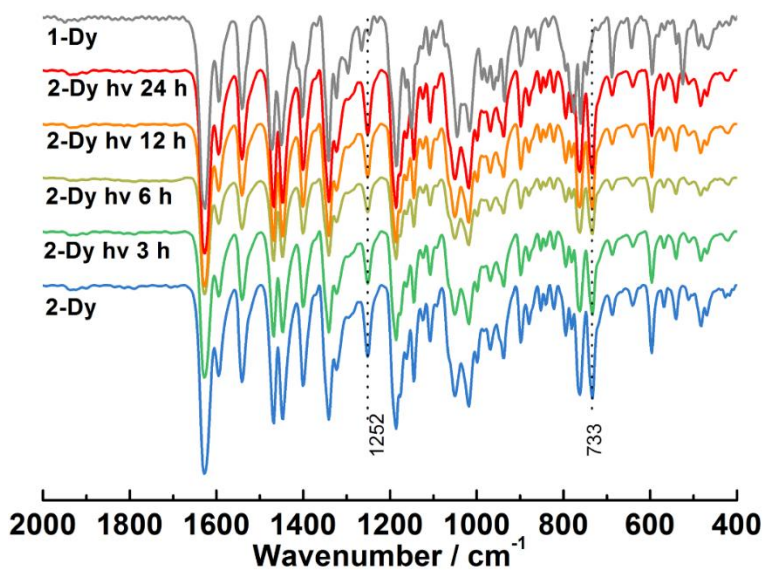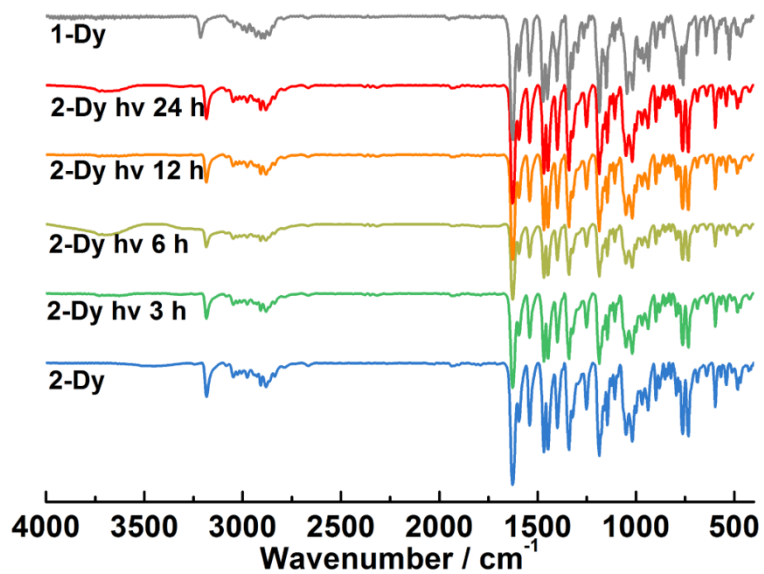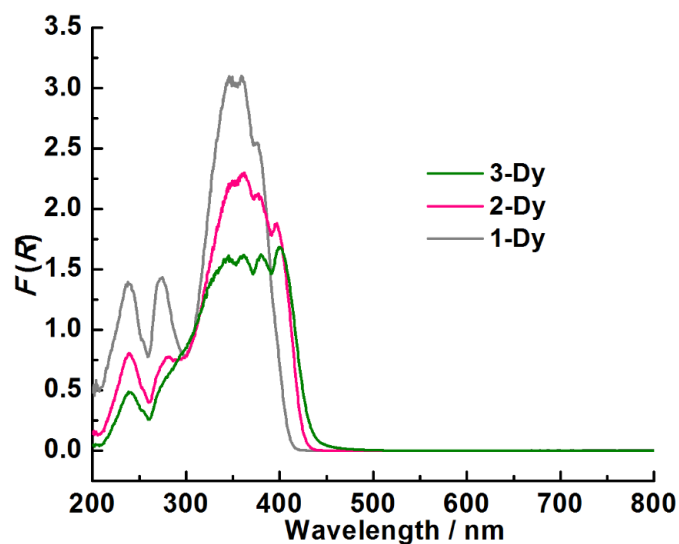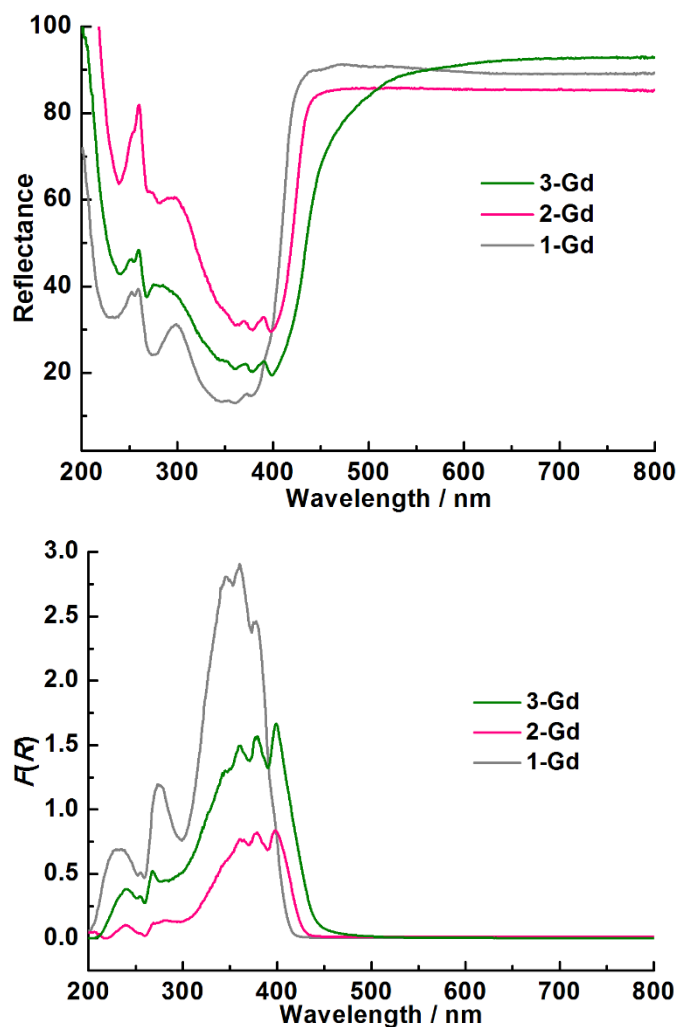
Figure S21. IR spectra of **1-Dy** (grey), **2-Dy** (blue) and **2-Dy** after UV light (λ = 365 nm) irradiation for different period of time.
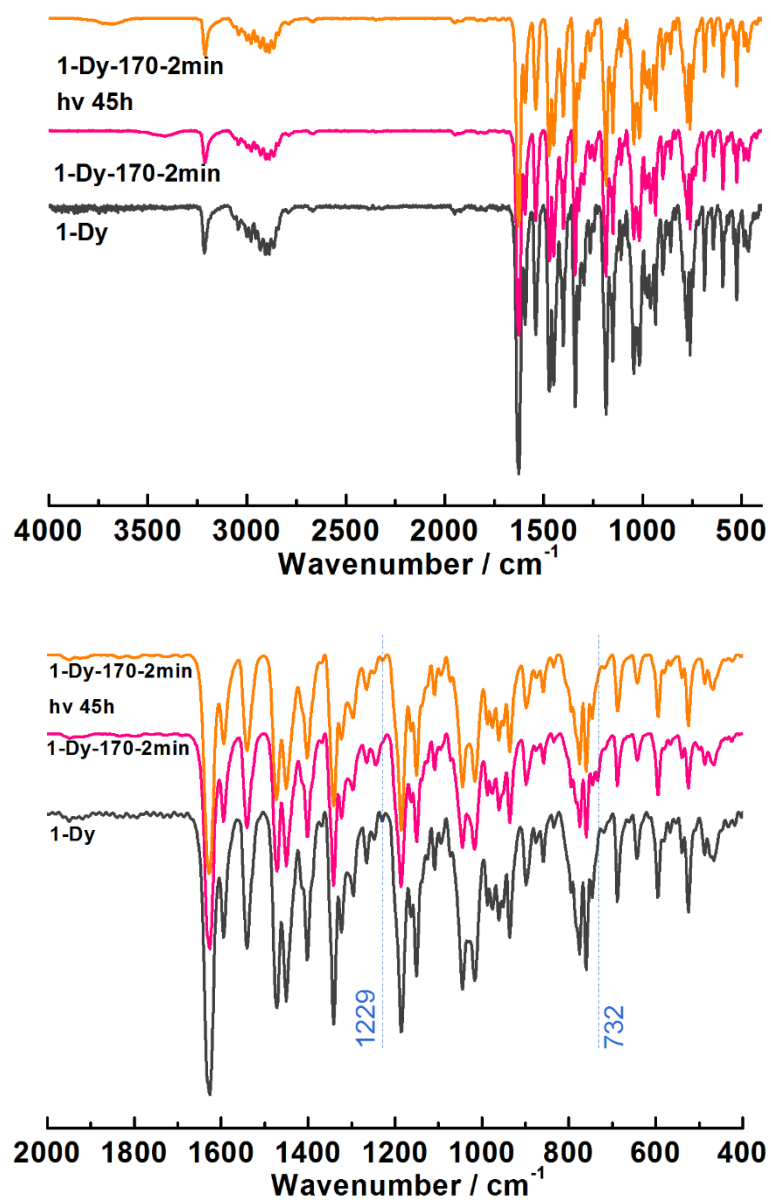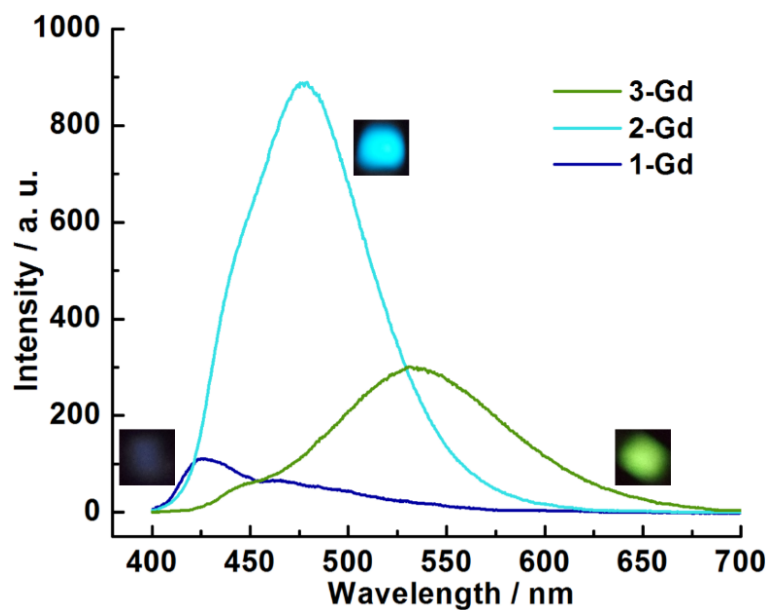
Figure S22. IR spectra of **1-Dy** (grey), **1-Dy-170-2min** (pink) and **1-Dy-170-2min** after UV light (λ = 365 nm) irradiation for 45 h (orange).
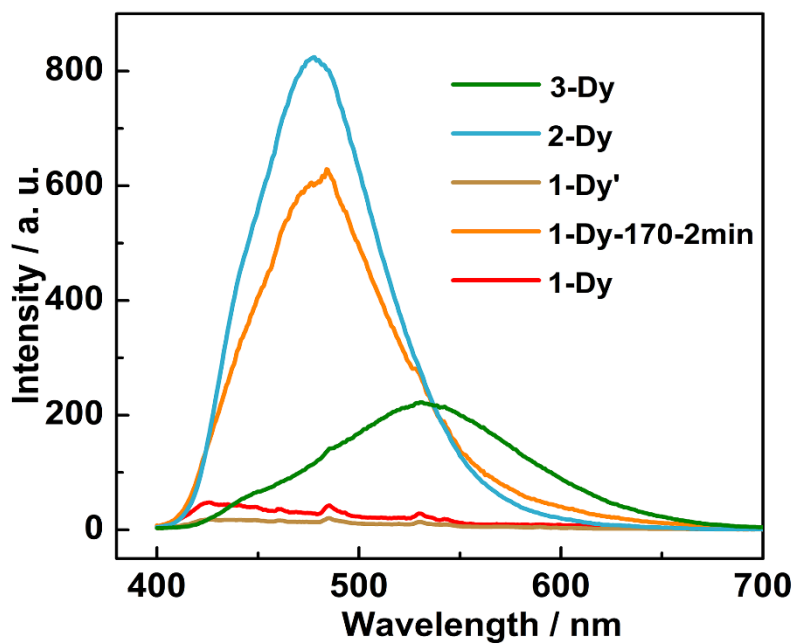
Figure S23. The transformed Kubelka–Munk function [F(R) = (1-R)^2/2R] (bottom) for compounds **1-Dy**, **2-Dy** and **3-Dy**.
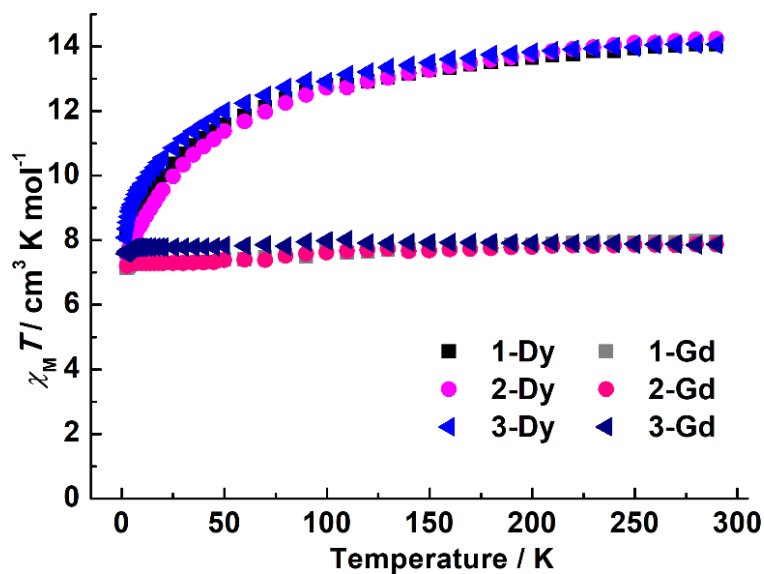

Figure S24. The UV-vis reflectance spectra (top) and transformed Kubelka–Munk function [F(R) = (1-R)^2/2R] (bottom) for compounds **1-Gd**, **2-Gd** and **3-Gd**.

Figure S25. The emission spectra excited at 310 nm for compounds **1-Gd**, **2-Gd** min and **3-Gd**. The inset shows corresponding luminescent pictures.


Figure S26. The emission spectra excited at 310 nm for **1-Dy**, **1-Dy-170-2min**, **1-Dy'**, **2-Dy** and **3-Dy**.

Figure S27. Temperature dependence of $\chi_M T$ on cooling in a field of 1 kOe for **1-Dy**, **2-Dy**, **3-Dy**, **1-Gd**, **2-Gd** and **3-Gd**. The $\chi_M T$ products at room temperature are 14.06, 14.23, 14.05, 7.96, 7.89 and 7.86 cm^3 K mol^{-1} for **1-Dy**, **2-Dy**, **3-Dy**, **1-Gd**, **2-Gd** and **3-Gd**.
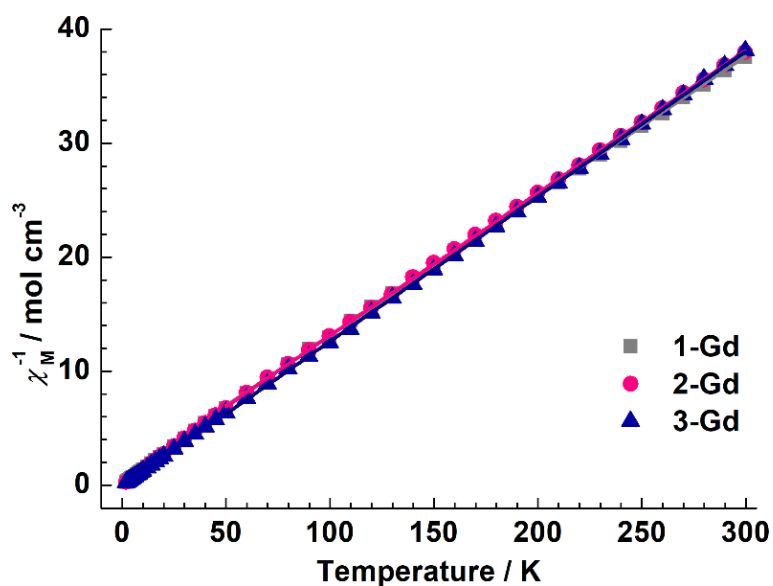

Figure S28. Temperature dependence of χ_M^{-1} on cooling in a field of 1 kOe for **1-Gd**, **2-Gd** and **3-Gd**. The solid lines represent the fits to Curie-Weiss law in temperature range of 50 – 300 K to attain Curie constant C of 8.15, 8.01 and 7.87 cm^3 K mol^{-1} and Weiss constant θ of -6.91, -5.28 and 0.72 K for compound **1-Gd**, **2-Gd** and **3-Gd**, respectively.
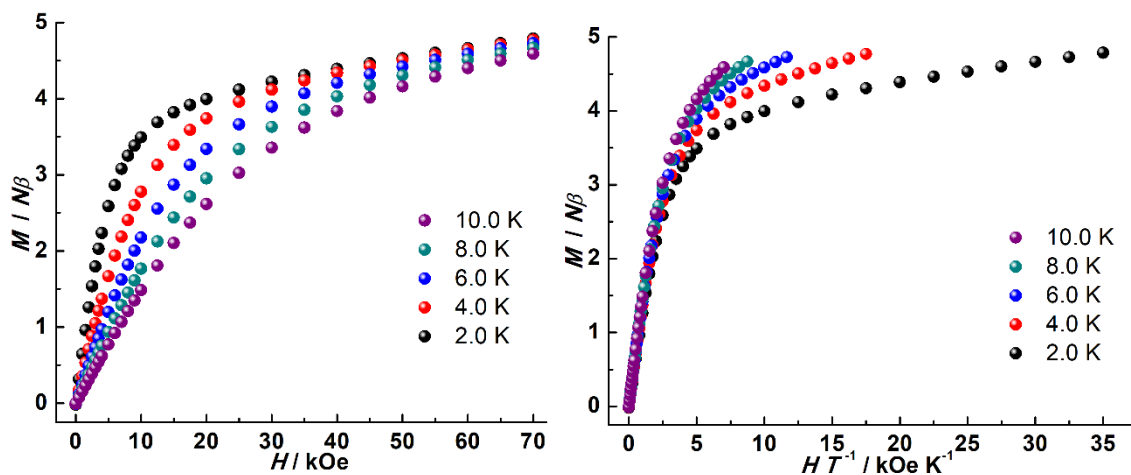
Figure S29. Field dependence of magnetization (left) and the plot of magnetization M versus H/T (right) at depicted temperatures for **1-Dy**.
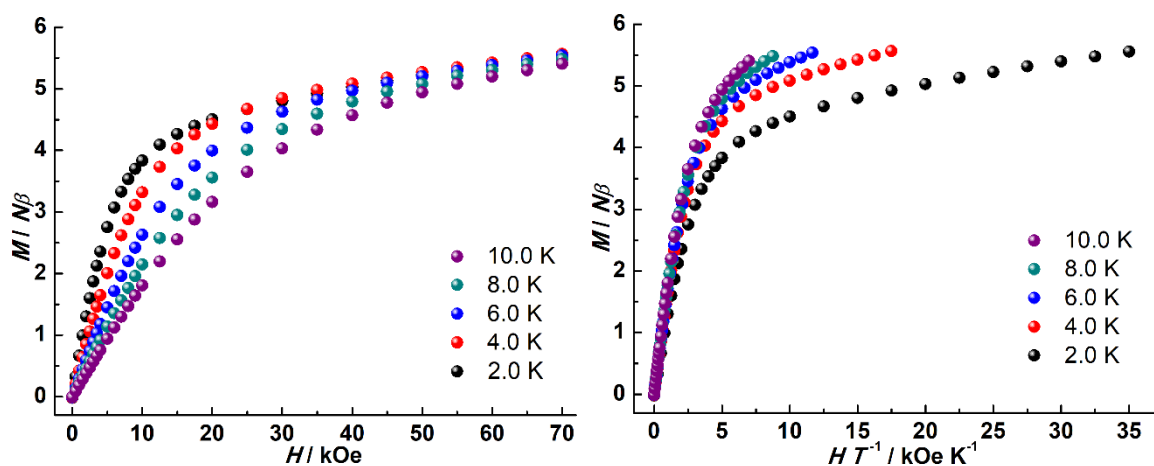

Figure S30. Field dependence of magnetization (left) and the plot of magnetization M versus H/T (right) at depicted temperatures for **2-Dy**.
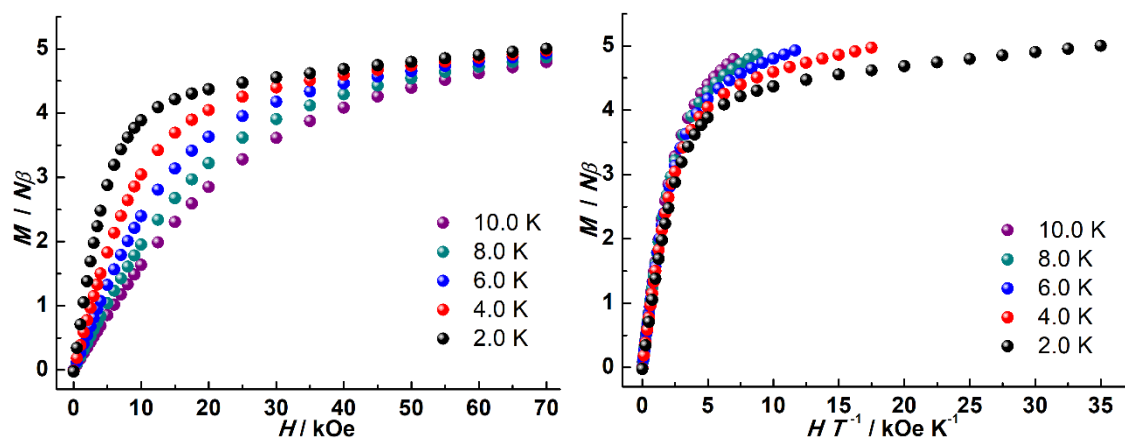

Figure S31. Field dependence of magnetization (left) and the plot of magnetization M versus H/T (right) at depicted temperatures for **3-Dy**.
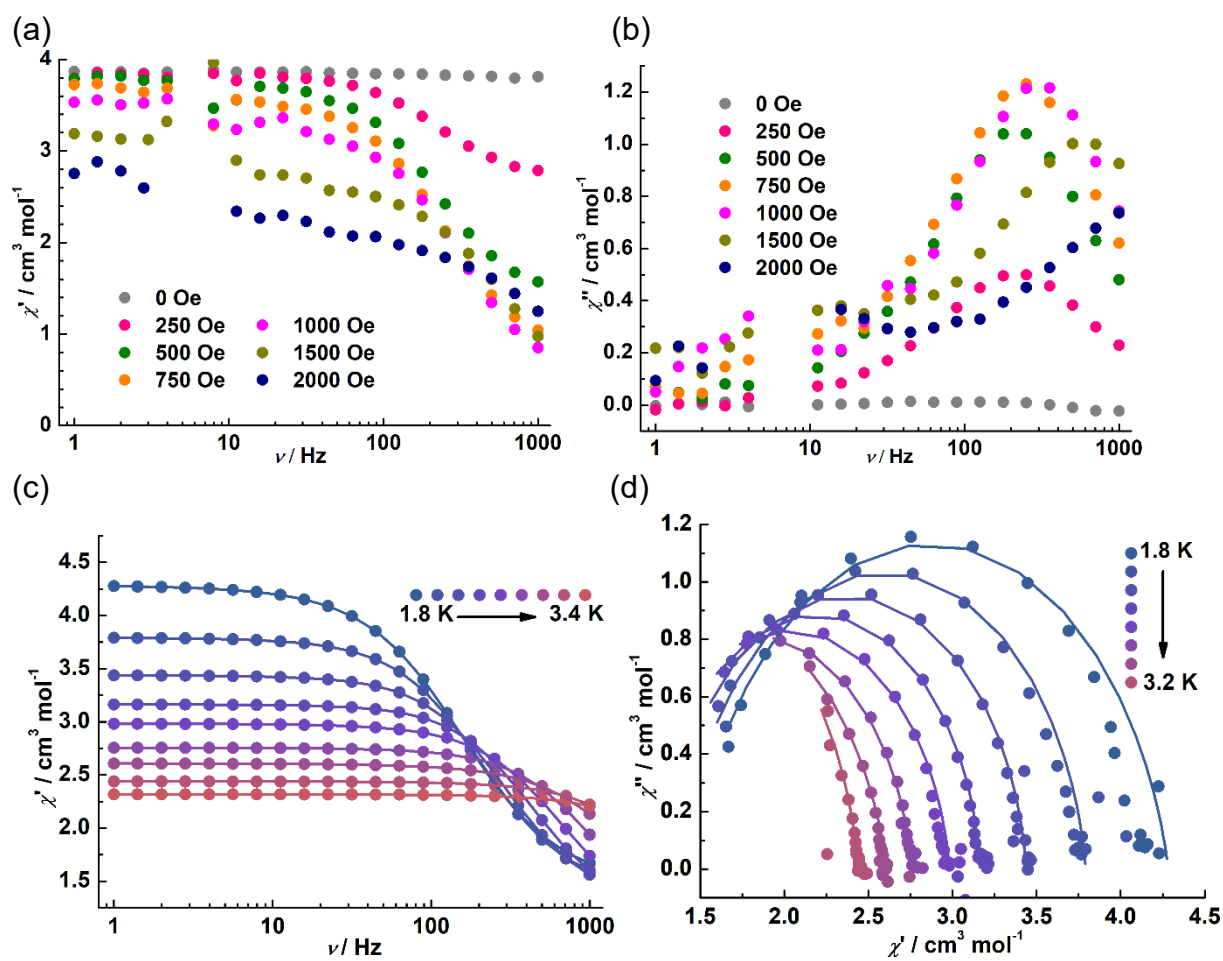
Figure S32. Frequency dependence of in-phase (χ', a) and out-of-phase (χ'', b) signals of **1-Dy** in the indicated dc fields at 2.0 K. Frequency dependence of the in-phase (χ', c) ac susceptibilities and Cole-Cole plots (d) for **1-Dy**, measured in the temperature range 1.8-3.4 K under 500 Oe dc field.
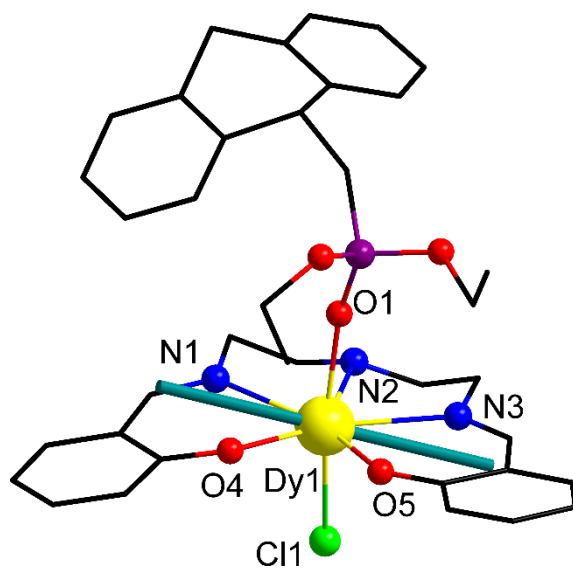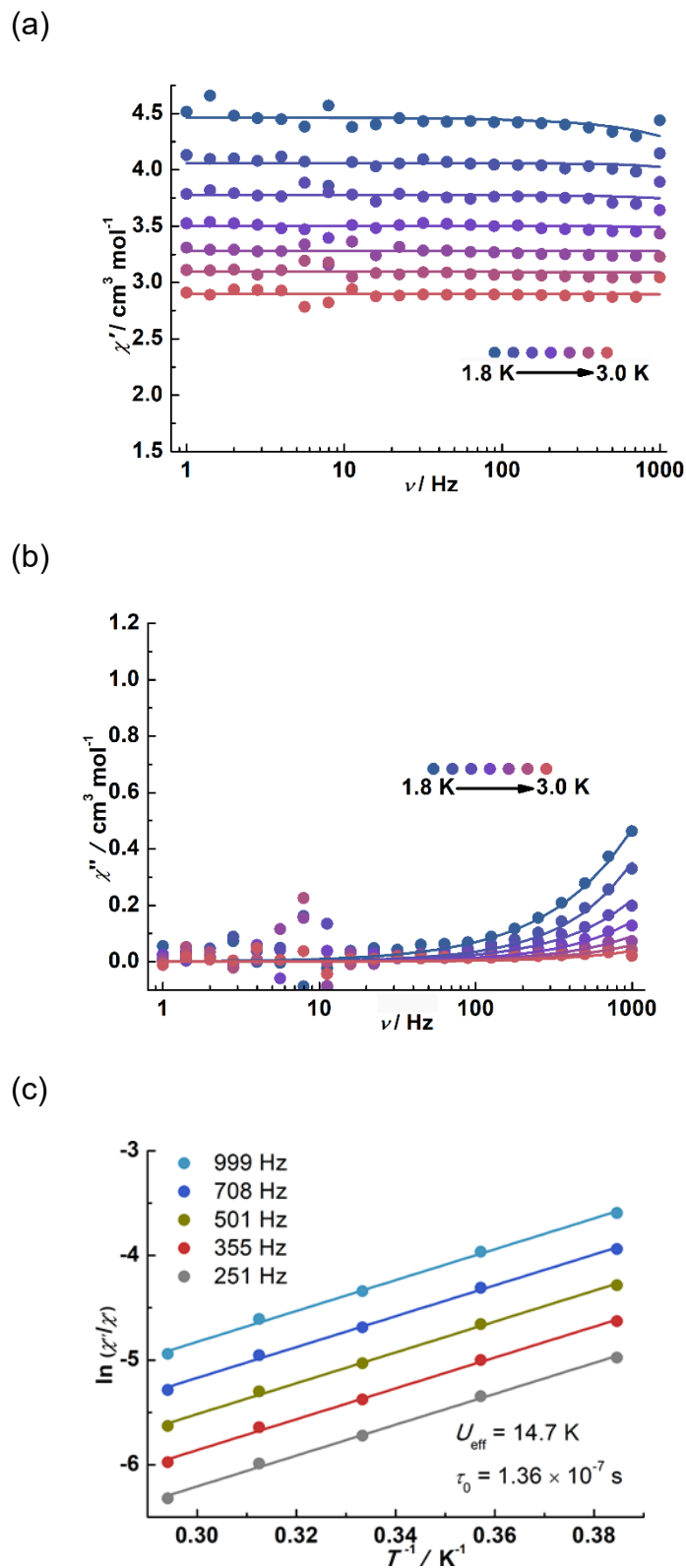
**Figure S33**. The electrostatic (cyan rod) anisotropy direction for the ground Kramers doublet in **1-Dy**.
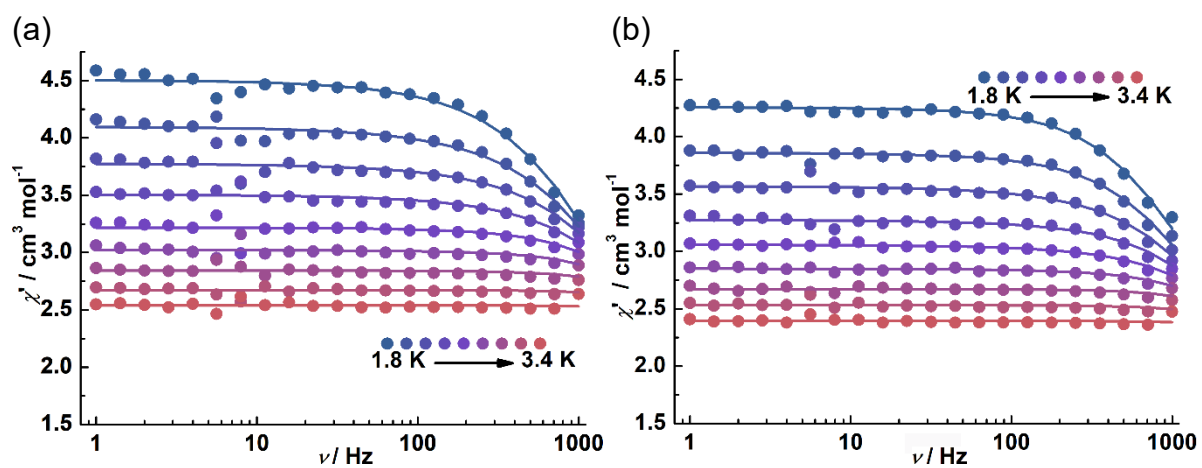
Figure S34. Frequency dependence of the in-phase (χ') ac susceptibilities for **1-Dy-170-2min** (a) and **2-Dy** (b) in a 500 Oe dc field.

Figure S35. Frequency dependence of the in-phase (χ', a) and out-of-phase (χ'', b) ac susceptibilities and corresponding plots of $\ln(\chi''/\chi')$ versus T^{-1} (c) for **3-Dy** measured in the temperature range 1.8 – 3.0 K under a 500 Oe dc field.
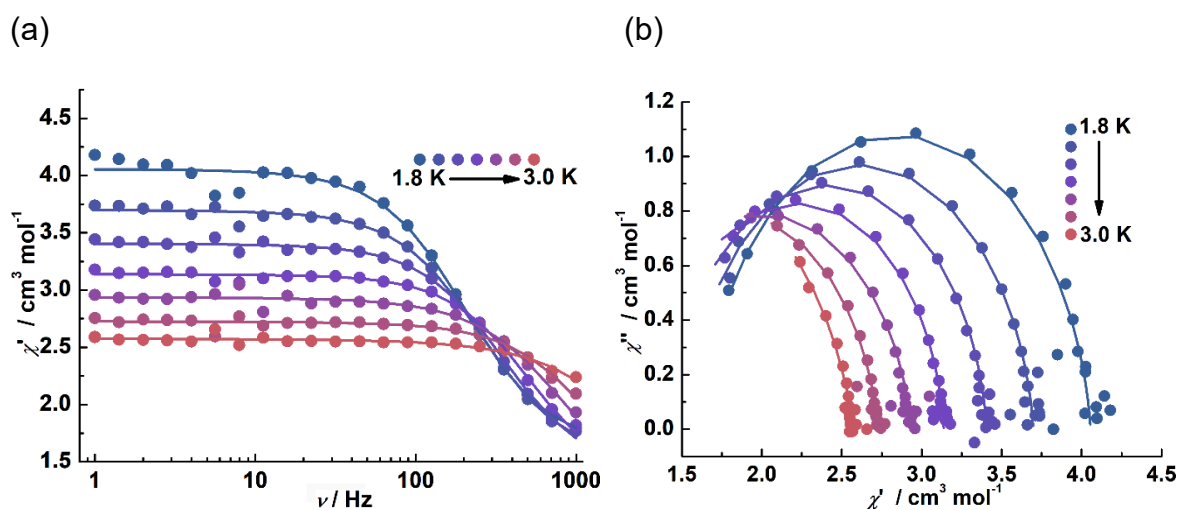
Figure S36. Frequency dependence of the in-phase (χ', a) ac susceptibilities and Cole-Cole plots (b) for **1-Dy'** under 500 Oe dc field.